Computational Mechanics manuscript No.
(will be inserted by the editor)

Fluid–structure interaction modeling of wind turbines: Simulating the full machine

Ming-Chen Hsu · Yuri Bazilevs

Received: 6 July 2012 / Accepted: date

Abstract In this paper we present our aerodynamics and fluid–structure interaction (FSI) computational techniques that enable dynamic, fully coupled, 3D FSI simulation of wind turbines at full scale, and in the presence of the nacelle and tower (i.e., simulation of the "full machine"). For the interaction of wind and flexible blades we employ a nonmatching interface discretization approach, where the aerodynamics is computed using a low-order finite-element-based ALE-VMS technique, while the rotor blades are modeled as thin composite shells discretized using NURBS-based isogeometric analysis (IGA). We find that coupling FEM and IGA in this manner gives a good combination of efficiency, accuracy, and flexibility of the computational procedures for wind turbine FSI. The interaction between the rotor and tower is handled using a non-overlapping sliding-interface approach, where both moving- and stationary-domain formulations of aerodynamics are employed. At the fluid–structure and sliding interfaces, the kinematic and traction continuity is enforced weakly, which is a key ingredient of the proposed numerical methodology.

We present several simulations of a three-blade 5 MW wind turbine, with and without the tower. We find that, in the case of no tower, the presence of the sliding interface has no effect on the prediction of aerodynamic loads on the rotor. From this we conclude that weak enforcement of the kinematics gives just as accurate results as the strong enforcement, and thus enables the simulation of rotor–tower interaction (as well as other applications involving mechanical components in relative motion). We also find that the blade passing the tower produces a 10%–12% drop (per blade) in the aerodynamic torque. We feel this finding may be important when it comes to the fatigue-life analysis and prediction for wind turbine blades.

Keywords NREL 5 MW offshore · wind turbine aerodynamics · fluid–structure interaction · ALE-VMS method · rotor–tower interaction · full machine · sliding-interface formulation

M.-C. Hsu · Y. Bazilevs (✉)
Department of Structural Engineering, University of California, San Diego, 9500 Gilman Drive, Mail Code 0085, La Jolla, CA 92093, USA
E-mail: yuri@ucsd.edu

1 Introduction

In the last several years there has been a significant increase in the research centered around aerodynamic and structural modeling of wind turbines. While most wind turbine aerodynamics and aeroelasticity simulations for engineering design are performed using low-fidelity methods (see, e.g., [1, 2]), there has been a growing body of research and development to raise the fidelity of wind turbine simulations. Standalone 3D computational fluid dynamics simulations of wind turbines may be found in [3–16], while standalone structural analyses of rotor blades of complex geometry and material composition under assumed or computed off-line wind load conditions are reported in [17–23]. In simulating wind turbine aerodynamics, only a handful of researchers (see, e.g., [7, 8, 13, 24]) considered full wind turbine simulations, where the wind turbine rotor, nacelle, and tower are all modeled. This is due to the additional computational challenges associated with the simulation of objects in relative motion.

Recently, a fully coupled fluid–structure interaction (FSI) simulation methodology for wind turbine rotors was developed in [25]. The simulations therein showed the importance of FSI modeling for full-scale wind turbine rotors. However, the FSI modeling in [25] only considered the interaction between the airflow and wind turbine rotor, without taking into account the tower and nacelle. In this paper we present our computational methodology to include the

tower and nacelle into the FSI modeling, which allows us to simulate the "full machine".

To enable the simulation of rotor–tower interaction, we adopt a sliding-interface formulation, which was first proposed in [26] and successfully tested on the NREL Phase VI wind turbine in [24]. We note that in application of the FEM to flows with moving mechanical components, the Shear–Slip Mesh Update Method [27–29] and its more general versions [30, 31] may also be employed to handle objects in relative motion. To handle the FSI we use a nonmatching interface discretization developed in [32], where we couple low-order FEM for aerodynamics and Isogeometric Analysis (IGA) [33,34] for structural mechanics. Using nonmatching discretizations at the fluid–structure interface can serve purposes beyond an implementation convenience typically associated with weakly-coupled FSI methods. What we do here is an example of taking advantage of the flexibility associated with using nonmatching discretizations, combining the most appropriate discretization for each part of an FSI problem. Exploiting this kind of flexibility, in conjunction with FSI homogenization methods [35–37], enabled computation of some of the most challenging parachute FSI problems [37–39], including parachute clusters [38, 39], where the contact model [39, 40] needed to deal with the interaction between the parachutes took advantage of this flexibility. Turbulence modeling in the aerodynamics formulation makes use of the recently proposed ALE-VMS technique [41,42] in combination with weakly enforced essential boundary conditions [43]. The latter greatly improve the accuracy of the ALE-VMS formulation in the presence of thin boundary layers near the rotor surface [44]. The Kirchhoff–Love shell formulation [45] in conjunction with the bending strip method [21] is used to model blade structures made of composite materials.

This paper is outlined as follows. In Section 2, we first state the continuum formulation of the FSI problem suitable for a nonmatching discretization of the fluid–structure interface. The fluid and structural mechanics formulations at the space-discrete level are shown next, followed by the presentation of the sliding-interface formulation. We conclude the section with a brief discussion of the time integration and FSI coupling techniques. In Section 3, we present the numerical results for the NREL 5 MW offshore wind turbine [2, 9]. We first verify that the aerodynamic loads are insensitive to the presence of the sliding interface. We then compute several cases to assess the importance of including FSI and rotor–tower interaction in the modeling. It is shown that both produce an appreciable effect. In Section 4, we draw conclusions and outline future developments.

2 Continuum and discrete modeling of FSI

In this section, we present the computational framework for fluid–structure interaction (FSI) analysis of a full wind turbine. For the FSI formulation we use the developments in [32]. The coupled FSI formulation is able to handle nonmatching fluid–structure interface discretizations without introducing the interface degrees-of-freedom. This is done for better efficiency of the computational procedures. To take into account the interaction between the rotor and tower, a non-overlapping sliding-interface method [24, 26] that handles subdomains in relative motion is also presented. The sliding-interface discretization also avoids the use of interface degrees-of-freedom.

2.1 FSI formulation at the continuum level suitable for nonmatching interface discretizations

Let $(\Omega_t)_1 \in \mathbb{R}^d$, $d = 2, 3$, represent the time-dependent domain of the fluid mechanics (or aerodynamics) problem with boundary $(\Gamma_t)_1$, let $(\Omega_t)_2 \in \mathbb{R}^d$ represent the time-dependent domain of the structural mechanics problem with boundary $(\Gamma_t)_2$, and let $(\Gamma_t)_\mathrm{I} \in \mathbb{R}^d$ represent the interface between the fluid and structural domains. Let $\mathbf{u}_1$ and p denote the fluid velocity and pressure, respectively, and let $\mathbf{u}_2$ denote the velocity of the structure. Let $\mathcal{S}_u$, $\mathcal{S}_p$, and $\mathcal{S}_d$ be the trial function spaces for the fluid velocity and pressure, and structural velocity, respectively, and $\mathcal{V}_u$, $\mathcal{V}_p$, and $\mathcal{V}_d$ be the corresponding test function spaces. The variational formulation for the coupled problem may be stated as: find $\mathbf{u}_1 \in \mathcal{S}_u$, $p \in \mathcal{S}_p$, and $\mathbf{u}_2 \in \mathcal{S}_d$, such that $\forall \mathbf{w}_1 \in \mathcal{V}_u$, $\forall q \in \mathcal{V}_p$, and $\forall \mathbf{w}_2 \in \mathcal{V}_d$,

$$
\begin{aligned}
&B_1(\{\mathbf{w}_1, q\}, \{\mathbf{u}_1, p\}; \hat{\mathbf{u}}) - F_1(\{\mathbf{w}_1, q\}) + B_2(\mathbf{w}_2, \mathbf{u}_2) - F_2(\mathbf{w}_2) \\
&- \int_{(\Gamma_t)_\mathrm{I}} (\mathbf{w}_1 - \mathbf{w}_2) \cdot \boldsymbol{\sigma}_1 (\mathbf{u}_1, p)\, \mathbf{n}_1 \, \mathrm{d}\Gamma \\
&- \int_{(\Gamma_t)_\mathrm{I}} \delta\boldsymbol{\sigma}_1 (\mathbf{w}_1, q)\, \mathbf{n}_1 \cdot (\mathbf{u}_1 - \mathbf{u}_2) \, \mathrm{d}\Gamma \\
&+ \int_{(\Gamma_t)_\mathrm{I}} (\mathbf{w}_1 - \mathbf{w}_2) \cdot \beta (\mathbf{u}_1 - \mathbf{u}_2) \, \mathrm{d}\Gamma = 0. \qquad (1)
\end{aligned}
$$

In the above, the subscripts 1 and 2 denote the fluid and structural mechanics quantities, and β is a penalty parameter, which we leave unspecified for the moment. Furthermore, B_1, F_1, B_2, and F_2 are the semilinear forms and linear functionals corresponding to the fluid and structural mechanics problems, and are given by

$$
\begin{aligned}
&B_1(\{\mathbf{w}, q\}, \{\mathbf{u}, p\}; \hat{\mathbf{u}}) \\
&= \int_{(\Omega_t)_1} \mathbf{w} \cdot \rho_1 \left(\left. \frac{\partial \mathbf{u}}{\partial t} \right|_{\hat{\mathbf{x}}} + (\mathbf{u} - \hat{\mathbf{u}}) \cdot \boldsymbol{\nabla} \mathbf{u} \right) \mathrm{d}\Omega
\end{aligned}
$$

$$+ \int_{(\Omega_t)_1} \boldsymbol{\varepsilon}(\mathbf{w}) : \boldsymbol{\sigma}_1(\mathbf{u}, p)\ \mathrm{d}\Omega + \int_{(\Omega_t)_1} q\boldsymbol{\nabla}\cdot\mathbf{u}\ \mathrm{d}\Omega, \tag{2}$$

$$F_1(\{\mathbf{w}, q\}) = \int_{(\Omega_t)_1} \mathbf{w}\cdot\rho_1\mathbf{f}_1\ \mathrm{d}\Omega + \int_{(\Gamma_t)_{1\mathrm{h}}} \mathbf{w}\cdot\mathbf{h}_1\ \mathrm{d}\Gamma, \tag{3}$$

$$B_2(\mathbf{w}, \mathbf{u}) = \int_{(\Omega_t)_2} \mathbf{w}\cdot\rho_2\frac{\mathrm{d}\mathbf{u}}{\mathrm{d}t}\ \mathrm{d}\Omega + \int_{(\Omega_t)_2} \boldsymbol{\varepsilon}(\mathbf{w}) : \boldsymbol{\sigma}_2(\mathbf{u})\ \mathrm{d}\Omega, \tag{4}$$

$$F_2(\mathbf{w}) = \int_{(\Omega_t)_2} \mathbf{w}\cdot\rho_2\mathbf{f}_2\ \mathrm{d}\Omega + \int_{(\Gamma_t)_{2\mathrm{h}}} \mathbf{w}\cdot\mathbf{h}_2\ \mathrm{d}\Gamma, \tag{5}$$

where ρ's are the densities, $\mathbf{f}$'s are the prescribed body forces, $\mathbf{h}$'s are the prescribed surface tractions, $\hat{\mathbf{u}}$ is the velocity of the fluid domain $(\Omega_t)_1$, $(\Gamma_t)_{1\mathrm{h}}$ and $(\Gamma_t)_{2\mathrm{h}}$ are the boundaries where the surface tractions are specified, $\big|_{\hat{\mathbf{x}}}$ denotes the fact that the time derivative in the fluid mechanics equations is taken with respect to the fixed referential domain spatial coordinates $\hat{\mathbf{x}}$, and $\frac{\mathrm{d}(\cdot)}{\mathrm{d}t}$ denotes the total time derivative (i.e., time derivative taken with respect to the fixed coordinates of the material configuration). The fluid mechanics Cauchy stress tensor $\boldsymbol{\sigma}_1$ is defined as

$$\boldsymbol{\sigma}_1(\mathbf{u}, p) = -p\mathbf{I} + 2\mu\boldsymbol{\varepsilon}(\mathbf{u}), \tag{6}$$

where $\mathbf{I}$ is the identity tensor, μ is the dynamic viscosity, and $\boldsymbol{\varepsilon}(\mathbf{u})$ is the strain-rate tensor given by

$$\boldsymbol{\varepsilon}(\mathbf{u}) = \frac{1}{2}\left(\boldsymbol{\nabla}\mathbf{u} + \boldsymbol{\nabla}\mathbf{u}^T\right). \tag{7}$$

In Eq. (1),

$$\delta\boldsymbol{\sigma}_1(\mathbf{w}, q)\,\mathbf{n} = 2\mu\boldsymbol{\varepsilon}(\mathbf{w})\mathbf{n} + q\mathbf{n}. \tag{8}$$

At this point we do not detail the structural Cauchy stress $\boldsymbol{\sigma}_2$ as we wish to keep the structural mechanics formulation flexible.

Remark 1 *The variational formulation given by Eq. (1) may be interpreted as Nitsche's method applied to the FSI problem (see, e.g., [46, 47]), or as a continuous version of the discontinuous Galerkin (DG) method (see, e.g., [48]) applied at the fluid–structure interface. It is assumed in Eq. (1) that the trial and test function spaces of the fluid and structural subproblems are independent of each other. This approach provides a framework that is capable of handling nonmatching fluid and structural interface discretizations.*

Remark 2 *If the fluid and structural velocities and the corresponding test functions are explicitly assumed to be continuous (i.e., $\mathbf{u}_1 = \mathbf{u}_2$ and $\mathbf{w}_1 = \mathbf{w}_2$) at the interface, the FSI formulation given by Eq. (1) reduces to a form suitable for matching fluid–structure interface meshes. Although somewhat limiting, matching interface discretizations were successfully applied to cardiovascular FSI in [49–57].*

2.2 ALE-VMS formulation of fluid mechanics with weak boundary conditions

We assume that the time-dependent fluid domain $(\Omega_t)_1$ is divided into N_{el} spatial subdomain elements denoted by $(\Omega_t^e)_1$. The fluid–structure interface $(\Gamma_t)_{\mathrm{I}}$ is decomposed into N_{eb} fluid domain surface elements denoted by Γ_t^b, and $(\Gamma_t)_{\mathrm{I}}^-$ is defined as the "inflow" part of $(\Gamma_t)_{\mathrm{I}}$. The discrete trial function spaces $\mathcal{S}_u^h$ for the velocity and $\mathcal{S}_p^h$ for the pressure, as well as the corresponding test function spaces $\mathcal{V}_u^h$ and $\mathcal{V}_p^h$ are assumed to be of equal order, and, in this work, are comprised of FEM functions. The discrete velocities and pressures and the corresponding test functions are now superscripted with h to denote their dependence on the mesh size.

The ALE-VMS formulation of the fluid mechanics subproblem, including the weakly enforced boundary conditions, is obtained by setting $\mathbf{w}_2 = \mathbf{0}$, $B_1 = B_1^{\mathrm{VMS}}$, $F_1 = F_1^{\mathrm{VMS}}$, and $\beta = \tau_{\mathrm{B}}$ in Eq. (1), and is given by: find $\mathbf{u}_1^h \in \mathcal{S}_u^h$ and $p^h \in \mathcal{S}_p^h$, such that $\forall\mathbf{w}_1^h \in \mathcal{V}_u^h$ and $\forall q^h \in \mathcal{V}_p^h$,

$$\begin{aligned}
&B_1^{\mathrm{VMS}}(\{\mathbf{w}_1^h, q^h\}, \{\mathbf{u}_1^h, p^h\}; \hat{\mathbf{u}}^h) - F_1^{\mathrm{VMS}}(\{\mathbf{w}_1^h, q^h\})\\
&- \sum_{b=1}^{N_{\mathrm{eb}}} \int_{\Gamma_t^b \cap (\Gamma_t)_{\mathrm{I}}} \mathbf{w}_1^h \cdot \boldsymbol{\sigma}_1\left(\mathbf{u}_1^h, p^h\right)\mathbf{n}_1\ \mathrm{d}\Gamma\\
&- \sum_{b=1}^{N_{\mathrm{eb}}} \int_{\Gamma_t^b \cap (\Gamma_t)_{\mathrm{I}}} \left(2\mu\boldsymbol{\varepsilon}\left(\mathbf{w}_1^h\right)\mathbf{n}_1 + q^h\mathbf{n}_1\right)\cdot\left(\mathbf{u}_1^h - \hat{\mathbf{u}}^h\right)\mathrm{d}\Gamma\\
&- \sum_{b=1}^{N_{\mathrm{eb}}} \int_{\Gamma_t^b \cap (\Gamma_t)_{\mathrm{I}}^-} \mathbf{w}_1^h \cdot \rho_1\left(\left(\mathbf{u}_1^h - \hat{\mathbf{u}}^h\right)\cdot\mathbf{n}_1\right)\left(\mathbf{u}_1^h - \hat{\mathbf{u}}^h\right)\mathrm{d}\Gamma\\
&+ \sum_{b=1}^{N_{\mathrm{eb}}} \int_{\Gamma_t^b \cap (\Gamma_t)_{\mathrm{I}}} \tau_{\mathrm{B}}\mathbf{w}_1^h \cdot \left(\mathbf{u}_1^h - \hat{\mathbf{u}}^h\right)\mathrm{d}\Gamma = 0,
\end{aligned} \tag{9}$$

where

$$\begin{aligned}
&B_1^{\mathrm{VMS}}(\{\mathbf{w}^h, q^h\}, \{\mathbf{u}^h, p^h\}; \hat{\mathbf{u}}^h) = B_1(\{\mathbf{w}^h, q^h\}, \{\mathbf{u}^h, p^h\}; \hat{\mathbf{u}}^h)\\
&+ \sum_{e=1}^{N_{\mathrm{el}}} \int_{(\Omega_t^e)_1} \tau_{\mathrm{M}}\left(\left(\mathbf{u}^h - \hat{\mathbf{u}}^h\right)\cdot\boldsymbol{\nabla}\mathbf{w}^h + \frac{\boldsymbol{\nabla}q^h}{\rho_1}\right)\cdot\mathbf{r}_{\mathrm{M}}\left(\mathbf{u}^h, p^h\right)\mathrm{d}\Omega\\
&+ \sum_{e=1}^{N_{\mathrm{el}}} \int_{(\Omega_t^e)_1} \rho_1\tau_{\mathrm{C}}\boldsymbol{\nabla}\cdot\mathbf{w}^h r_{\mathrm{C}}\left(\mathbf{u}^h, p^h\right)\mathrm{d}\Omega\\
&- \sum_{e=1}^{N_{\mathrm{el}}} \int_{(\Omega_t^e)_1} \tau_{\mathrm{M}}\mathbf{w}^h \cdot \left(\mathbf{r}_{\mathrm{M}}\left(\mathbf{u}^h, p^h\right)\cdot\boldsymbol{\nabla}\mathbf{u}^h\right)\mathrm{d}\Omega\\
&- \sum_{e=1}^{N_{\mathrm{el}}} \int_{(\Omega_t^e)_1} \frac{\boldsymbol{\nabla}\mathbf{w}^h}{\rho_1} : \left(\tau_{\mathrm{M}}\mathbf{r}_{\mathrm{M}}\left(\mathbf{u}^h, p^h\right)\right)\otimes\left(\tau_{\mathrm{M}}\mathbf{r}_{\mathrm{M}}\left(\mathbf{u}^h, p^h\right)\right)\mathrm{d}\Omega,
\end{aligned} \tag{10}$$

and

$$F_1^{\mathrm{VMS}}(\{\mathbf{w}^h, q^h\}) = F_1(\{\mathbf{w}^h, q^h\}). \tag{11}$$

In the above equations, $\hat{\mathbf{u}}^h$ is the mesh velocity, and $\mathbf{r}_{\mathrm{M}}$ and r_{C} are the residuals of the momentum and continuity equations, respectively, given by

$$\mathbf{r}_{\mathrm{M}}(\mathbf{u}^h, p^h) = \rho_1 \left(\left.\frac{\partial \mathbf{u}^h}{\partial t}\right|_{\hat{\mathbf{x}}} + \left(\mathbf{u}^h - \hat{\mathbf{u}}^h\right) \cdot \boldsymbol{\nabla} \mathbf{u}^h - \mathbf{f}^h \right) - \boldsymbol{\nabla} \cdot \boldsymbol{\sigma}_1 \left(\mathbf{u}^h, p^h\right), \tag{12}$$

and

$$r_{\mathrm{C}}(\mathbf{u}^h, p^h) = \boldsymbol{\nabla} \cdot \mathbf{u}^h. \tag{13}$$

The definitions of τ_{M} and τ_{C}, the stabilization parameters, may be found in [50, 58–67]).

The ALE-VMS method is a moving-domain extension of the residual-based variational multiscale (RBVMS) formulation proposed in [66] in the context of nonmoving domain problems. Weakly enforced essential boundary conditions were introduced in [43], which improved the performance of the ALE-VMS formulation in the presence of underresolved boundary layers [68–70]. The definition of the boundary stabilization (or penalty) parameter τ_{B} may be found in [44].

In the case of FSI, the essential boundary conditions for the fluid mechanics problem at the fluid–structure interface come from the structural velocity. In this case, the mesh velocity $\hat{\mathbf{u}}^h$ on $(\Gamma_t)_{\mathrm{I}}$ may be computed as

$$\hat{\mathbf{u}}^h = \Pi_1^h \mathbf{u}_2^h, \tag{14}$$

where Π_1^h is a projection or interpolation operator onto the space spanned by the basis functions of the fluid mechanics problem restricted to the fluid–structure interface. In this work we use an L^2-projection. Equation (14) gives the coupling to the structural mechanics problem, which is discussed in the next section.

2.3 Kirchhoff–Love shell formulation of structural mechanics and the bending strip method

The discrete variational formulation of the structural mechanics problem is obtained by setting $\{\mathbf{w}_1, q\} = \{\mathbf{0}, 0\}$ in Eq. (1) and assuming that the structure is governed by the isogeometric Kirchhoff–Love composite shell formulation with the aid of the bending strip method [21, 25, 45]. The shell midsurface is described using a piecewise smooth (C^1- or higher-order continuous) geometrical mapping. Regions where the mapping reduces to the C^0 level are also allowed. This includes situations where the shell surface geometry is described using several NURBS patches that are joined with C^0-continuity. For this reason, we define $(\Gamma_2^{\mathrm{s}})_0$ and $(\Gamma_2^{\mathrm{s}})_t$ to be the structure midsurface, which is composed of the structural patches or subdomains, in the reference and deformed configuration, respectively. Furthermore, $(\Gamma_2^{\mathrm{b}})_0$ denotes the bending strip domain, which is a union of the bending strip patch subdomains, in the reference configuration.

Let $\mathcal{S}_d^h$ and $\mathcal{V}_d^h$ denote the discrete trial and test function spaces for the structural mechanics problem. The rotation-free Kirchhoff–Love shell formulation may be stated as: find the velocity of the shell midsurface $\mathbf{u}_2^h \in \mathcal{S}_d^h$, such that for all test functions $\mathbf{w}_2^h \in \mathcal{V}_d^h$,

$$\begin{aligned} &\int_{(\Gamma_t^{\mathrm{s}})_2} \mathbf{w}_2^h \cdot \rho_2 h_{\mathrm{th}} \left(\frac{\mathrm{d}\mathbf{u}_2^h}{\mathrm{d}t} - \mathbf{f} \right) \mathrm{d}\Gamma \\ &+ \int_{(\Gamma_0^{\mathrm{s}})_2} \delta\bar{\boldsymbol{\epsilon}}^h \cdot \left(\mathbf{A}\, \bar{\boldsymbol{\epsilon}}^h + \mathbf{B}\, \bar{\boldsymbol{\kappa}}^h \right) \mathrm{d}\Gamma \\ &+ \int_{(\Gamma_0^{\mathrm{s}})_2} \delta\bar{\boldsymbol{\kappa}}^h \cdot \left(\mathbf{B}\, \bar{\boldsymbol{\epsilon}}^h + \mathbf{D}\, \bar{\boldsymbol{\kappa}}^h \right) \mathrm{d}\Gamma \\ &+ \int_{(\Gamma_0^{\mathrm{b}})_2} \delta\bar{\boldsymbol{\kappa}}^h \cdot \mathbf{D}_{\mathrm{b}}\, \bar{\boldsymbol{\kappa}}^h \, \mathrm{d}\Gamma - \int_{(\Gamma_t)_{\mathrm{I}}} \mathbf{w}_2^h \cdot (\Pi_2^h \mathbf{t}_1^h) \, \mathrm{d}\Gamma = 0. \end{aligned} \tag{15}$$

In the above, h_{th} is the shell thickness, $\bar{\boldsymbol{\epsilon}}^h$ and $\bar{\boldsymbol{\kappa}}^h$ are the tensors of membrane strains and curvature changes in Voigt notation written with respect to the local Cartesian basis oriented on the first covariant basis vector of the midsurface, $\delta\bar{\boldsymbol{\epsilon}}^h$ and $\delta\bar{\boldsymbol{\kappa}}^h$ are their variations, $\mathbf{A}$, $\mathbf{B}$ and $\mathbf{D}$ are the membrane, coupling and bending stiffnesses, respectively, pre-integrated through the thickness, $\mathbf{D}_{\mathrm{b}}$ is the bending stiffness of the bending strips, Π_2^h is an L^2-projection operator onto the space spanned by the basis functions of the structural mechanics problem restricted to the fluid–structure interface, and $\mathbf{t}_1^h$ is the discrete fluid traction given by

$$\mathbf{t}_1^h = -\boldsymbol{\sigma}_1^h \mathbf{n}_1 - \tau_{\mathrm{B}} \left(\mathbf{u}_2^h - \mathbf{u}_1^h \right). \tag{16}$$

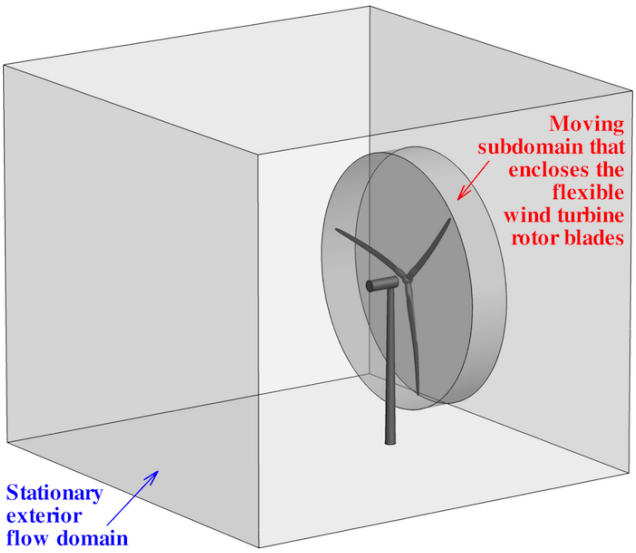

Fig. 1 Setup for the simulation of a full machine. The interior moving subdomain, which encloses the wind turbine rotor, and the exterior stationary subdomain, which houses the nacelle and tower, are shown.

Although NURBS are employed in this work to discretize the structural mechanics equations, T-splines [71,72] or subdivision surfaces [73–75] are also well suited for the proposed structural modeling approach. For alternative rotation-free shell formulations the reader is referred to [73–79].

2.4 Sliding-interface formulation for objects in relative motion

In order to simulate the full wind turbine configuration and investigate the rotor–tower interaction, we consider an approach that makes use of a moving subdomain, which encloses the entire wind turbine rotor, and a stationary subdomain that contains the rest of the wind turbine (see Figure 1). The two domains are in relative motion and share a sliding cylindrical interface. The meshes on each side of the interface are nonmatching because of the relative motion (see Figure 2). As a result, a numerical procedure is needed to impose the continuity of the kinematics and tractions at the stationary and rotating subdomain interface despite the fact that the interface discretizations are incompatible. Such a procedure was developed in [26] in the context of IGA for computing flows about rotating components. The advantage of IGA for rotating-component flows is that the cylindrical sliding interfaces are represented exactly and no geometry errors are incurred. In the case of standard FEM employed here, the geometric compatibility is only approximate. The sliding-interface coupling was successfully tested on the NREL Phase VI wind turbine in [24] and is presented in what follows.

Let the subscripts 1S and 1M denote the quantities pertaining to the fluid mechanics problem on the stationary and moving subdomains, respectively. The subdomain that encloses the rotor rotates with it, and the interior of the rotating subdomain is allowed to deflect to accommodate the motion of the blades. However, the motion of the outer boundary of the rotor subdomain is restricted to a rigid rotation to maintain geometric compatibility with the stationary subdomain. To enforce the compatibility of the flow kinematics and tractions at the sliding interface, we add the following terms to the ALE-VMS formulation given by Eq. (9):

$$
\begin{aligned}
&-\sum_{b=1}^{N_{\text{eb}}} \int_{\Gamma_t^b \bigcap (\Gamma_t)_{\text{SI}}} \left(\mathbf{w}_{1\text{S}}^h - \mathbf{w}_{1\text{M}}^h\right) \cdot \frac{1}{2} \left(\boldsymbol{\sigma}_{1\text{S}} \mathbf{n}_{1\text{S}} - \boldsymbol{\sigma}_{1\text{M}} \mathbf{n}_{1\text{M}}\right) \mathrm{d}\Gamma \\
&-\sum_{b=1}^{N_{\text{eb}}} \int_{\Gamma_t^b \bigcap (\Gamma_t)_{\text{SI}}} \frac{1}{2} \left(\delta\boldsymbol{\sigma}_{1\text{S}} \mathbf{n}_{1\text{S}} - \delta\boldsymbol{\sigma}_{1\text{M}} \mathbf{n}_{1\text{M}}\right) \cdot \left(\mathbf{u}_{1\text{S}}^h - \mathbf{u}_{1\text{M}}^h\right) \mathrm{d}\Gamma \\
&-\sum_{b=1}^{N_{\text{eb}}} \int_{\Gamma_t^b \bigcap (\Gamma_t)_{\text{SI}}} \mathbf{w}_{1\text{S}}^h \cdot \rho \left\{\left(\mathbf{u}_{1\text{S}}^h - \hat{\mathbf{u}}_{1\text{S}}^h\right) \cdot \mathbf{n}_{1\text{S}}\right\}_- \left(\mathbf{u}_{1\text{S}}^h - \mathbf{u}_{1\text{M}}^h\right) \mathrm{d}\Gamma \\
&-\sum_{b=1}^{N_{\text{eb}}} \int_{\Gamma_t^b \bigcap (\Gamma_t)_{\text{SI}}} \mathbf{w}_{1\text{M}}^h \cdot \rho \left\{\left(\mathbf{u}_{1\text{M}}^h - \hat{\mathbf{u}}_{1\text{M}}^h\right) \cdot \mathbf{n}_{1\text{M}}\right\}_- \left(\mathbf{u}_{1\text{M}}^h - \mathbf{u}_{1\text{S}}^h\right) \mathrm{d}\Gamma \\
&+\sum_{b=1}^{N_{\text{eb}}} \int_{\Gamma_t^b \bigcap (\Gamma_t)_{\text{SI}}} \frac{C_{\text{I}}^{\text{B}} \mu}{h_n} \left(\mathbf{w}_{1\text{S}}^h - \mathbf{w}_{1\text{M}}^h\right) \cdot \left(\mathbf{u}_{1\text{S}}^h - \mathbf{u}_{1\text{M}}^h\right) \mathrm{d}\Gamma = 0, \quad (17)
\end{aligned}
$$

where $\delta\boldsymbol{\sigma}$ is given by Eq. (8), $(\Gamma_t)_{\text{SI}}$ is the sliding interface, and $\{\mathcal{A}\}_-$ denotes the negative part of $\mathcal{A}$, that is, $\{\mathcal{A}\}_- = \mathcal{A}$ if $\mathcal{A} < 0$ and $\{\mathcal{A}\}_- = 0$ if $\mathcal{A} \geq 0$. Just as in the FSI case, the sliding-interface formulation may be see as a DG method, where the continuity of the basis function is enforced everywhere in the interior of the two subdomains, but not at the sliding interface between them. The structure of the terms on the sliding interface is similar to that of the weak enforcement of essential boundary conditions (see Eq. (9)). The significance of each term is explained in detail in [26]. Note that, in the current application, $\hat{\mathbf{u}}_{1\text{S}}^h = \mathbf{0}$, because the subdomain 1S is stationary. However, the formulation is able to handle situations where both subdomains are in motion.

Remark 3 *Nonmatching interface discretizations in the FSI and sliding-interface problems necessitate the use of interpolation or projection of kinematic and traction data between the nonmatching surface meshes (see, e.g., [32, 80–82], where [82] is more comprehensive than [81]). A computational procedure, which can simultaneously handle the data transfer for IGA and FEM discretizations, was proposed in [32]. The procedure also includes a robust approach in identifying "closest points" for arbitrary shaped surfaces. While such interface projections are rather straightforward for weakly-coupled FSI algorithms, they require special techniques [40, 65, 82] for strongly-coupled, "direct" and "quasi-direct" methods [40, 65, 82–84] that are monolithic-like (i.e. become monolithic for matching discretizations).*

2.5 Time integration of the FSI equations and coupling

The ALE formulation for fluid mechanics and the Lagrangian formulation for structural mechanics give a natural setting for a finite-difference time integration of this coupled FSI system. In this work, we employ the Generalized-α technique [50,85,86], which is a fully-implicit second-order accurate method with control over the dissipation of high-frequency modes. At each time step the combined fluid, structure and mesh motion discrete residuals are converged to zero by means of a block-iterative FSI coupling approach [65,83,84]. The block-iterative approach for nonconforming fluid and structural meshes consists of the following sequence of linear solves. We first compute the fluid mechanics solution increment holding the structural and mesh solutions fixed. We then update the fluid solution, extract the

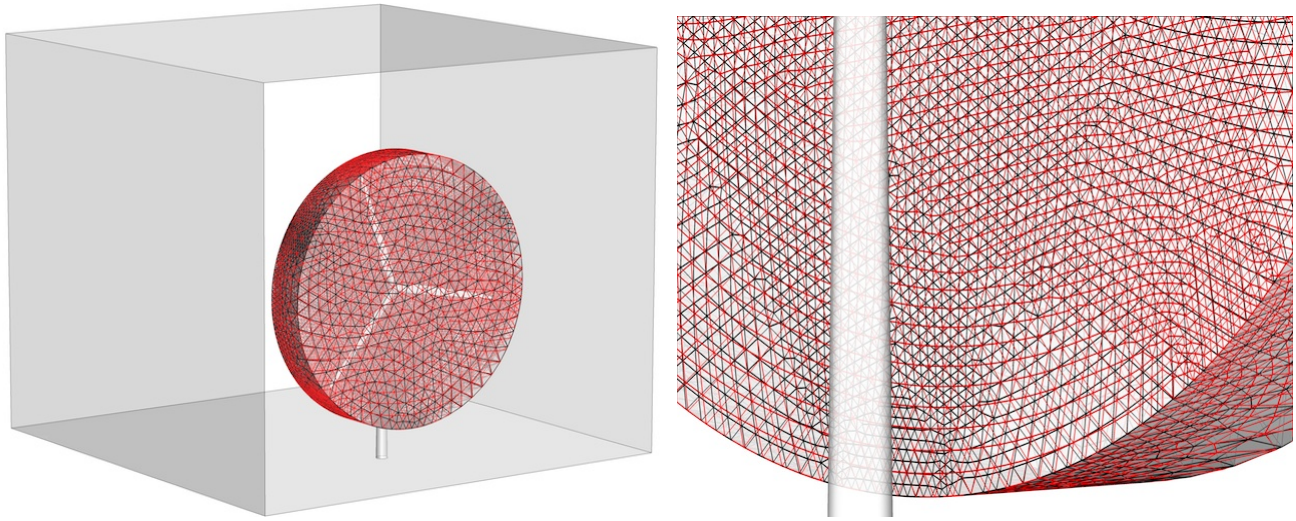

Fig. 2 Nonmatching meshes at the sliding interface between the stationary and moving subdomains.

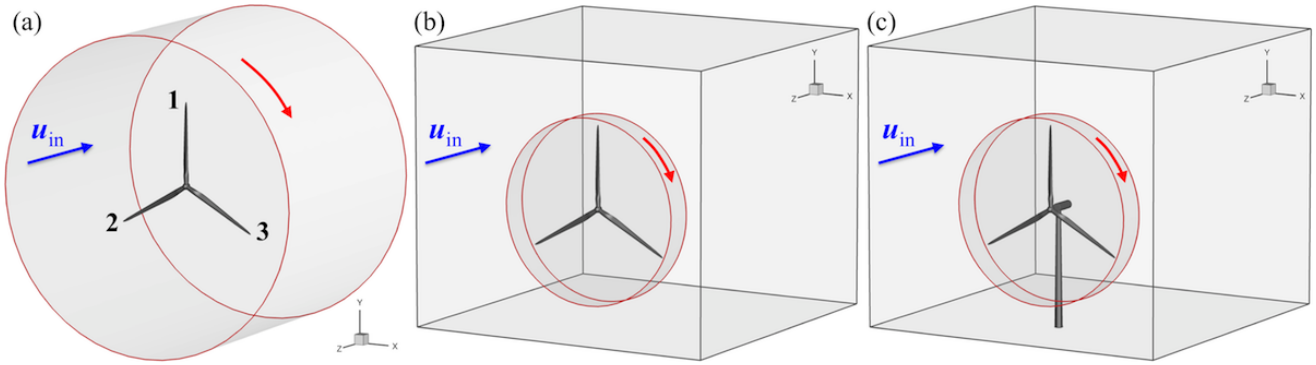

Fig. 3 Cases considered. (a) Case I: Rotor only. (b) Case II: Rotor only, including a sliding interface. (c) Case III: Full machine with a sliding interface.

fluid traction and project it to the structure, and obtain the structural mechanics solution increment. Finally, we update the structural solution, project the structural kinematics data to the fluid domain boundary, and update the mesh solution increment using the linear elasticity operator. This three-step iteration sequence is repeated until convergence to an appropriately coupled discrete solution is achieved. We note that only the mesh motion part associated with blade deflections is computed using the mesh moving method that we typically use, which is an elastic mesh moving technique with Jacobian-based stiffening [87–89]. The mesh motion part associated with blade rotations is computed exactly (see [25] for details). The block-iterative approach to FSI coupling is stable and efficient for wind turbine simulation.

Table 1 Mesh statistics for Cases I, II and III.

	Number of Nodes	Number of Elements
Case I	1,319,427	4,218,459
Case II	1,326,129	4,205,519
Case III	1,440,425	4,828,692

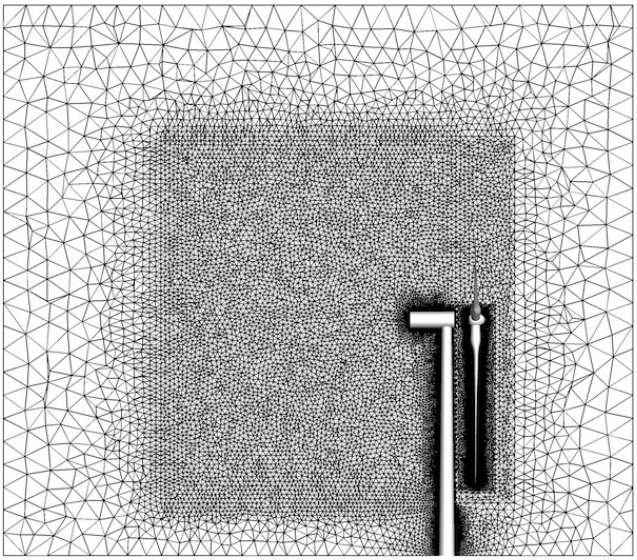

Fig. 4 A 2D cut at $x = 0$ to show the mesh quality used in Case III. The mesh is refined in the inner region for better flow resolution near the wind turbine.

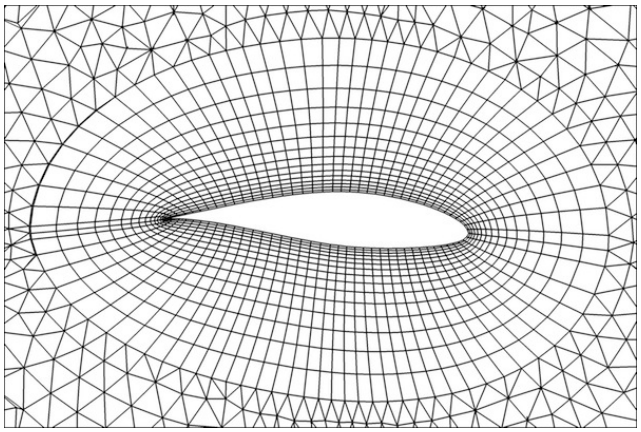

Fig. 5 A 2D cut at 75% spanwise station to illustrate the boundary-layer mesh. The size of the first element in the wall-normal direction is 0.02 m, and a growth ratio of 1.2 is used to generate 15 layers of prismatic elements.

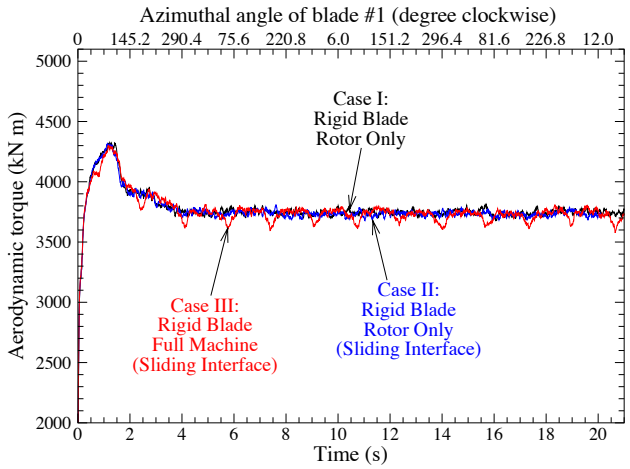

Fig. 6 The aerodynamic torque for the rigid-blade computations. For the full-machine simulation, the torque drops when the blade passes in front of the tower.

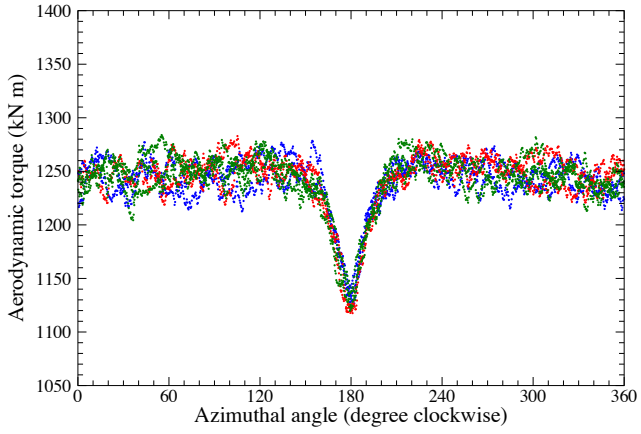

Fig. 7 The single-blade aerodynamic torque as a function of the azimuthal angle for a rigid-blade full-machine simulation. The 180° angle corresponds to the instant when the blade passes in front the tower. At that instant the predicted drop in the torque is 10%–12% of its computed value when the blade is away from the tower.

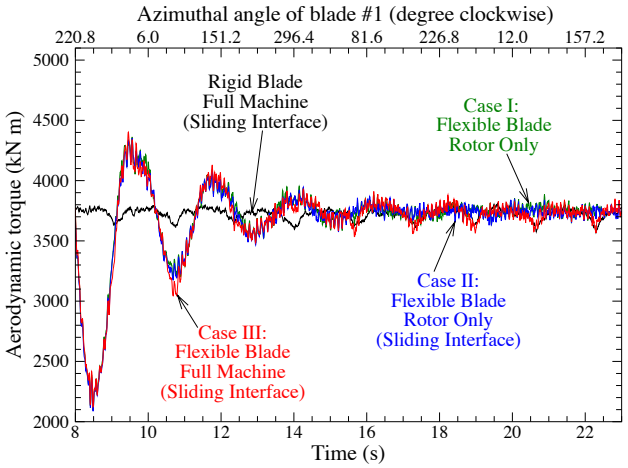

Fig. 8 The aerodynamic torque for flexible-blade FSI computations.

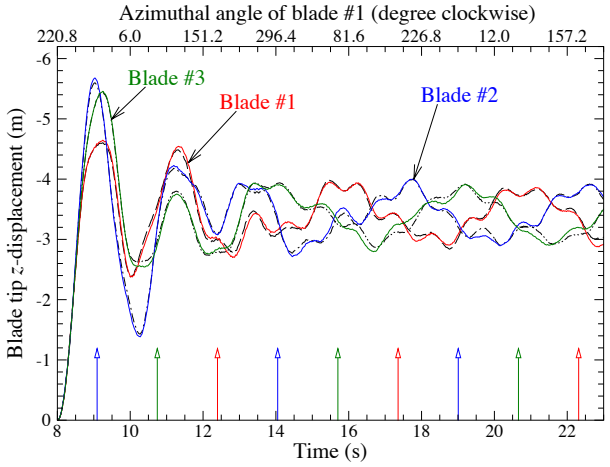

Fig. 9 The blade tip z-displacement for rotor-only (dashed, dashed-dotted, and dashed-dotted-dotted lines) and full-machine (solid lines) simulations. The arrows near the bottom of the figure show the instants where the blade passes in front of the tower.

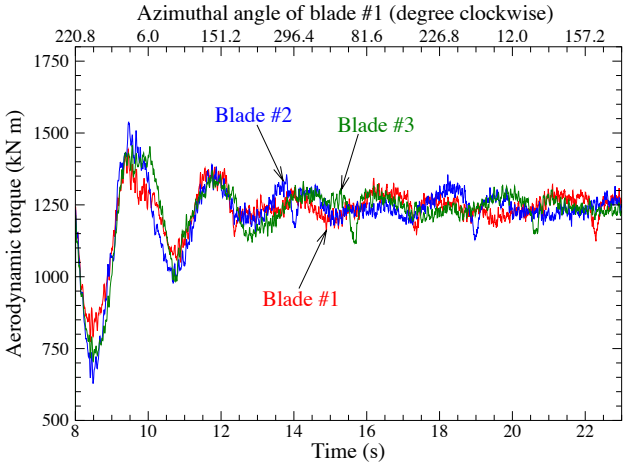

Fig. 10 The aerodynamic torque of individual blades for flexible-blade full-machine simulation.

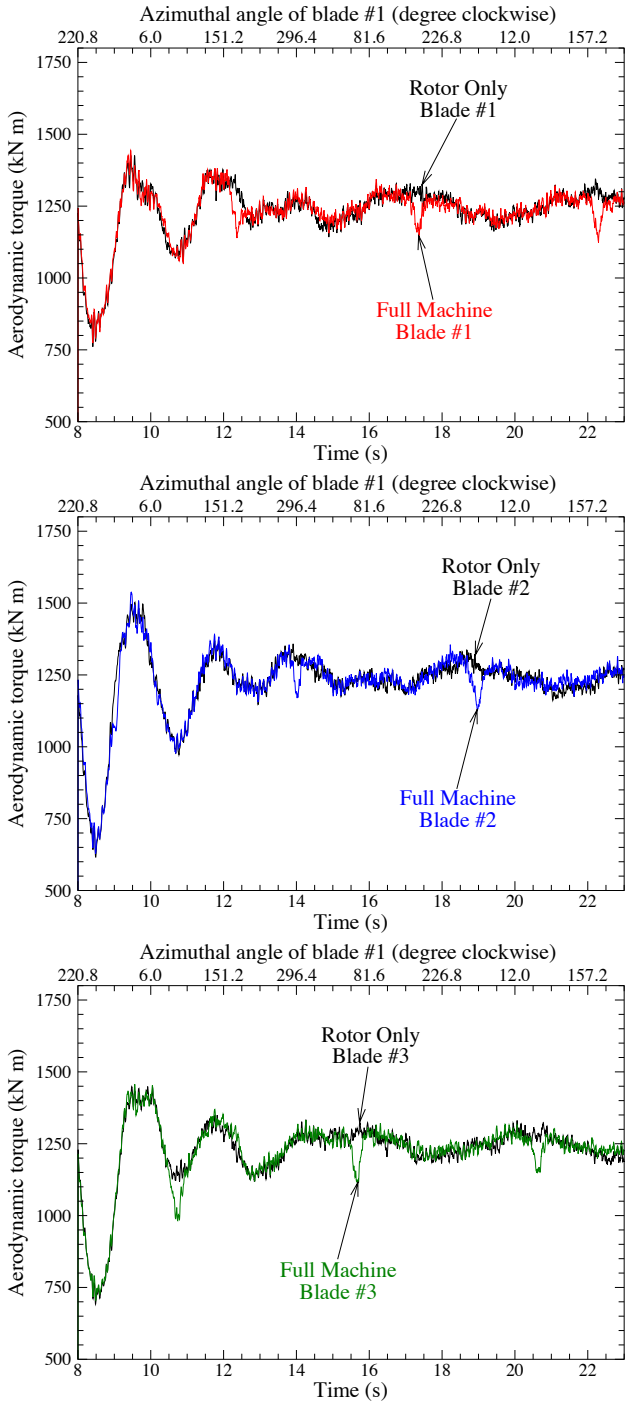

Fig. 11 The aerodynamic torque of individual blades for rotor-only and full-machine simulations (flexible blade). The drop in the aerodynamic torque is clearly visible.

3 Computational results

In this section, we present our computations of the NREL 5 MW offshore baseline wind turbine [2, 9]. The NREL 5 MW wind turbine is a conventional three-blade upwind turbine proposed in [2] to support concept studies aimed at assessing offshore wind technology [90–96]. The rotor-only configuration of this wind turbine was simulated earlier in [9–11, 25, 32, 41, 44, 97] using both NURBS-based IGA and standard FEM. The detailed geometry description and construction for the blade surface was documented in [9]. The 63 m blade is composed of a series of DU airfoils and the NACA64 profile. In this work, the proposed framework is applied to the simulation of the full wind turbine configuration, including the rotor (blades and hub), nacelle, and tower. The land-based tower is assumed to be rigid, and has a base diameter of 6 m and a top diameter of 3.87 m. The tower height is 87.6 m and the hub height is 90 m [2].

The cases considered in this work are show in Figure 3. Case I is a rotor-only setup, where the rotor is enclosed in a cylindrical domain, and the rotation is applied to the entire computational domain to simulate the spinning rotor. Case II is also a rotor-only setup, however, the rotor is housed in a cylindrical rotating subdomain that is enclosed by a stationary exterior flow subdomain. The sliding-interface formulation is applied at the interface between the subdomains to weakly impose the continuity of the kinematics and tractions. We compare the simulation results from Cases I and II to study the effect of the sliding-interface formulation. Case III has a similar setup as Case II, but this time the stationary subdomain contains the nacelle and tower, and thus enables us to study the rotor–tower interaction effects.

All simulations are performed at the rated wind speed of 11.4 m/s and a fixed rotor speed of 12.1 rpm. This setup corresponds to one of the cases reported in [2]. The wind speed is prescribed at the inflow boundary, the traction vector is set to zero at the outflow boundary, and the slip condition is set on the top, bottom, and lateral boundaries. The air density and viscosity are 1.2 kg/m^3 and 2.0×10^{-5} kg/(m s), respectively.

The aerodynamics volume mesh statistics for all three cases are summarized in Table 1. Case III has more elements and nodes compared with Cases I and II due to the presence of the nacelle and tower. A 2D cut of the mesh at $x = 0$ for Case III is shown in Figure 4 to show the mesh quality used in our computations. The mesh is refined in the inner region for better flow resolution. Figure 5 shows a 2D cut at 75% spanwise station to illustrate the boundary-layer mesh used in our computations. Near the blade surface, the size of the first element in the wall-normal direction is 0.02 m, and 15 layers of prismatic elements were generated with a growth ration of 1.2. The Reynolds number based on the chord length and relative speed at this location is $O(10^7)$. The same boundary-layer mesh is used in all three cases. The time-step size is 2.5×10^{-4} s for all cases. Both rigid- and flexible-blade computations are performed for each case.

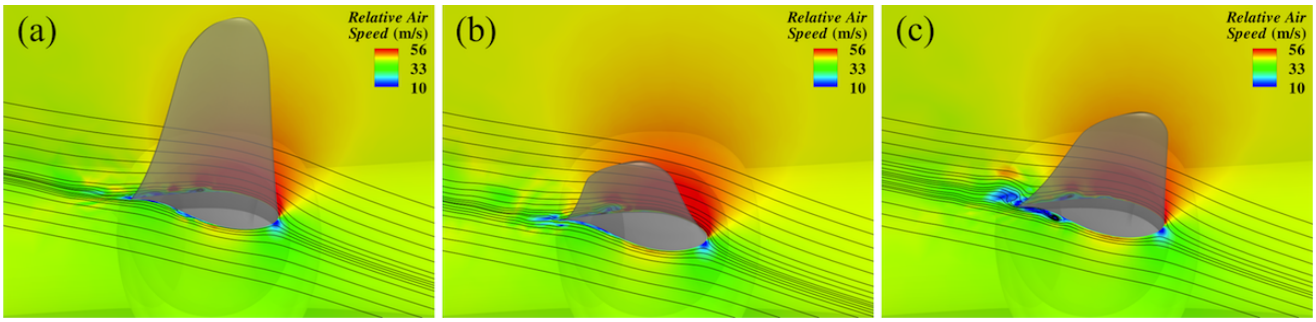

Fig. 12 Relative air speed and streamlines at 50% spanwise station, rotated to the reference configuration, and superposed on the moving blade #2 at three different time instants: (a) t = 9.0 s, (b) t = 10 s, and (c) t = 12.5 s.

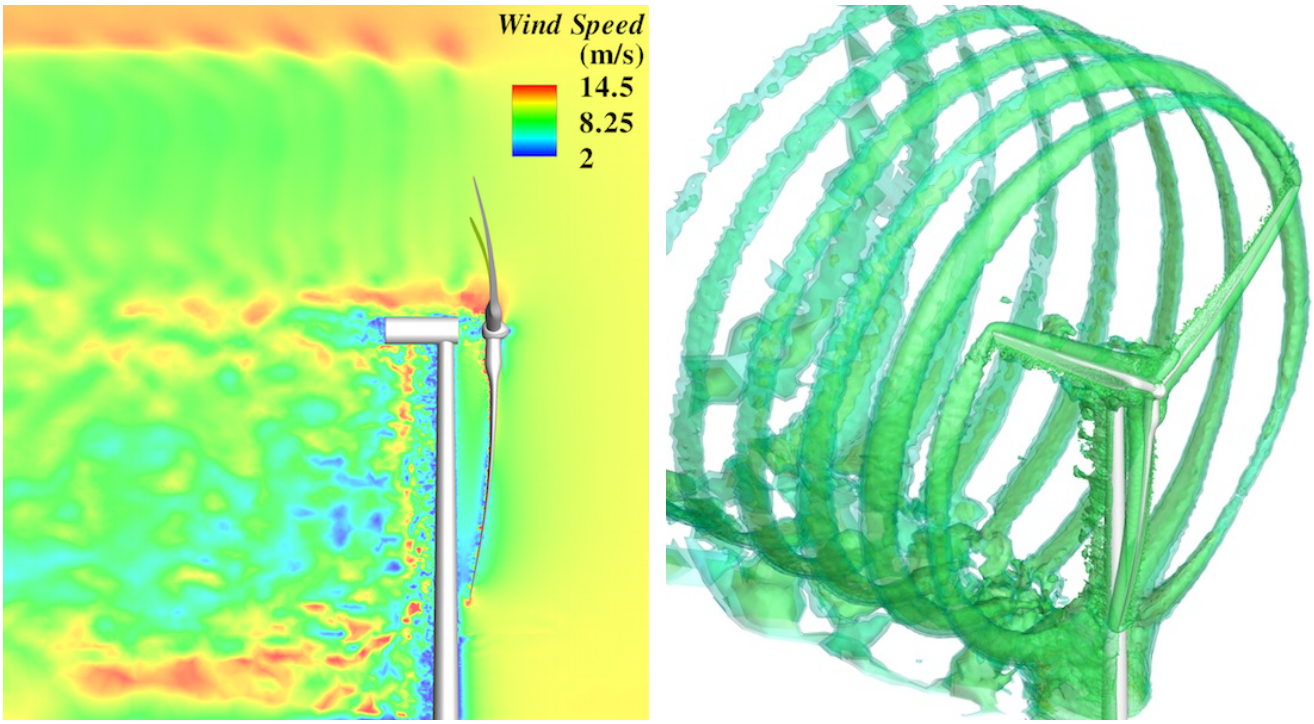

Fig. 13 Air speed contours at a planar cut (left) and isosurfaces of air speed (right) at an instant for the flexible-blade full-machine simulation.

Table 2 Time-averaged (over one revolution) aerodynamic torques

	Rigid-Blade Aerodynamic Torque (kN m)	Flexible-Blade Aerodynamic Torque (kN m)
Case I	3735	3749
Case II	3733	3751
Case III	3716	3734

3.1 Rigid-blade simulations

We first perform the simulations assuming the rotor blades are rigid. The time history of the aerodynamic torque is plotted in Figure 6 for all three cases. The comparison between Case I and II shows that the presence of the sliding interface has no effect on the prediction of aerodynamic loads on the rotor. From this we conclude that weak enforcement of the kinematics at the sliding interface gives just as accurate results as the strong enforcement, and thus enables the simulation of rotor–tower interaction (as well as other applications involving mechanical components in relative motion).

Figure 6 also shows the time history of the aerodynamic torque for Case III, where the nacelle and tower are included and the full machine is considered in the simulation. The results clearly show several "dips" in the torque history, each dip corresponding to one of the blades passing the tower. To better examine the tower effect, we plot the aerodynamic torque for each individual blade as a function of the azimuthal angle (see Figure 7). For each blade, the azimuthal angle of 180° represents the instant when the blade passes the tower. At that instant the predicted drop in the torque is 10%–12% of its computed value when the blade is away from the tower. This finding may be important when

it comes to the fatigue-life analysis and prediction for wind turbine blades.

3.2 Flexible-blade simulations

The rotor blades are discretized using NURBS-based IGA. A symmetric fiberglass/epoxy composite with $[\pm 45/0/90_2/0_3]_s$ lay-up was proposed in [25] for the blade material. The details of the NURBS structure model, including the homogenization of the material and the laminate thickness distributions, can be found in [25, 98]. There are 4897 control points in the quadratic NURBS mesh.

We perform FSI (flexible-blade) simulations for all three cases. The time history of the aerodynamic torques are shown in Figure 8. The comparison between Cases I and II again shows that the presence of the sliding interface has no effect on the prediction of aerodynamic loads on the rotor. We also note the transient dynamic effect as well as high frequency oscillations in the FSI curves compared with the rigid-blade simulation result. The tower effect is still appreciable.

Figure 9 shows the tip z-displacement history of the individual blades. The solid lines are the results from Case III (full machine), while the dashed, dashed-doted, and dashed-doted-doted lines are from Case II (rotor only). From the comparison we note that the rotor–tower interaction doesn't seem to produce a pronounced response in the blade tip displacement.

Figure 10 shows the aerodynamic torques of individual blades for Case III. Note that the torque histories are clearly different between three blades. From Figures 9 and 10 we also note that the individual tip displacement and torque do not settle at the steady values. Once the initial transient decays, the tip displacement varies between 3 and 4 m during one revolution. The dynamic effect is also present in individual torque curves shown in Figure 10. After the initial transient decays, the torque varies between 1180 and 1330 kN m during one revolution. Figure 11 compares the torque history of individual blades between Cases II and III to show the effect of rotor–tower interaction in FSI computations. The drop in aerodynamic torque is clearly seen for all three blades.

Figure 12 shows the relative air speed and streamlines at 50% spanwise station, rotated to the reference configuration, and superposed on the moving blade #2. The blade mostly displaces in the flapwise direction, however, the edgewise displacement may also be observed. The weak enforcement of boundary conditions results in the flow slipping on the solid surface. Figure 13 shows the flow visualization of the full wind turbine configuration. The tip vortex decays very slowly as it is convected downstream. Note that no visible discontinuities are seen in the flow field at the sliding interface, which indicates that the method correctly handles the kinematic compatibility at this location.

The time-averaged aerodynamic torque values for all cases are summarized in Table 2. From the FSI computation of Case III, and without considering any power loss, the energy generated by this wind turbine design is about 4.73 MW. According to the Betz' law (see, e.g. [99]), the maximum power that this wind turbine design is able to extract for the wind and rotor speeds considered is 6.57 MW, leading to the aerodynamic efficiency of 72%, which is quite good for modern wind turbine designs.

4 Conclusions

We presented our aerodynamics and FSI computational techniques that enable dynamic, fully coupled, 3D FSI simulation of wind turbines at full scale, and in the presence of the nacelle and tower (i.e., simulation of the "full machine"). The structural modeling of wind turbine blades makes use of the isogeometric rotation-free shell formulation, which is coupled to the low-order finite-element-based ALE-VMS technique for aerodynamics. This presents a good combination of accuracy and efficiency of the wind turbine FSI simulations. The blade–tower interaction is successfully handled using a sliding-interface technique with weak enforcement of flow kinematic and traction compatibility.

The computational results indicate that the blade passing the tower produces an appreciable drop in the aerodynamic torque. This creates additional cyclic loading on the blades that may be important when it comes to their fatigue-life analysis. Furthermore, the FSI modeling employed in this work captures the variability in the deformation of the individual blades as well as that of the aerodynamic torque during one revolution. Because at any instant in time the blade deformation is nonsymmetric, this creates eccentric loads on the hub, which may be important to predict for the purposes of hub and nacelle design.

Acknowledgements The support of the NSF CAREER Award No. 1055091 is gratefully acknowledged. We thank the Texas Advanced Computing Center (TACC) at the University of Texas at Austin and the San Diego Supercomputing Center (SDSC) at the University of California, San Diego for providing HPC resources that have contributed to the research results reported in this paper.

References

1. J. M. Jonkman and M. L. Buhl Jr. FAST user's guide. Technical Report NREL/EL-500-38230, National Renewable Energy Laboratory, Golden, CO, 2005.
2. J. Jonkman, S. Butterfield, W. Musial, and G. Scott. Definition of a 5-MW reference wind turbine for offshore system development. Technical Report NREL/TP-500-38060, National Renewable Energy Laboratory, Golden, CO, 2009.

3. N. N. Sørensen, J. A. Michelsen, and S. Schreck. Navier–Stokes predictions of the NREL Phase VI rotor in the NASA Ames 80 ft × 120 ft wind tunnel. *Wind Energy*, 5:151–169, 2002.
4. E. P. N. Duque, M. D. Burklund, and W. Johnson. Navier–Stokes and comprehensive analysis performance predictions of the NREL Phase VI experiment. *Journal of Solar Energy Engineering*, 125:457–467, 2003.
5. A. Le Pape and J. Lecanu. 3D Navier–Stokes computations of a stall-regulated wind turbine. *Wind Energy*, 7:309–324, 2004.
6. D. D. Chao and C. P. van Dam. Computational aerodynamic analysis of a blunt trailing-edge airfoil modification to the NREL Phase VI rotor. *Wind Energy*, 10:529–550, 2007.
7. S. Gómez-Iradi, R. Steijl, and G. N. Barakos. Development and validation of a CFD technique for the aerodynamic analysis of HAWT. *Journal of Solar Energy Engineering*, 131:031009–1–13, 2009.
8. F. Zahle, N. N. Sørensen, and J. Johansen. Wind turbine rotor-tower interaction using an incompressible overset grid method. *Wind Energy*, 12:594–619, 2009.
9. Y. Bazilevs, M.-C. Hsu, I. Akkerman, S. Wright, K. Takizawa, B. Henicke, T. Spielman, and T. E. Tezduyar. 3D simulation of wind turbine rotors at full scale. Part I: Geometry modeling and aerodynamics. *International Journal for Numerical Methods in Fluids*, 65:207–235, 2011.
10. K. Takizawa, B. Henicke, T. E. Tezduyar, M.-C. Hsu, and Y. Bazilevs. Stabilized space–time computation of wind-turbine rotor aerodynamics. *Computational Mechanics*, 48:333–344, 2011.
11. K. Takizawa, B. Henicke, D. Montes, T. E. Tezduyar, M.-C. Hsu, and Y. Bazilevs. Numerical-performance studies for the stabilized space–time computation of wind-turbine rotor aerodynamics. *Computational Mechanics*, 48:647–657, 2011.
12. A. Bechmann, N. N. Sørensen, and F. Zahle. CFD simulations of the MEXICO rotor. *Wind Energy*, 14:677–689, 2011.
13. Y. Li and P. M. Carrica K. J. Paik, T. Xing. Dynamic overset CFD simulations of wind turbine aerodynamics. *Renewable Energy*, 37:285–298, 2012.
14. N. N. Sørensen and S. Schreck. Computation of the National Renewable Energy Laboratory Phase-VI rotor in pitch motion during standstill. *Wind Energy*, 2012. doi:10.1002/we.480.
15. F. Scheurich and R. E. Brown. Modelling the aerodynamics of vertical-axis wind turbines in unsteady wind conditions. *Wind Energy*, 2012. doi:10.1002/we.532.
16. R. Chow and C. P. van Dam. Verification of computational simulations of the NREL 5 MW rotor with a focus on inboard flow separation. *Wind Energy*, 2012. doi:10.1002/we.529.
17. C. Kong, J. Bang, and Y. Sugiyama. Structural investigation of composite wind turbine blade considering various load cases and fatigue life. *Energy*, 30:2101–2114, 2005.
18. E. Lund and J. Stegmann. On structural optimization of composite shell structures using a discrete constitutive parametrization. *Wind Energy*, 8:109–124, 2005.
19. M. O. L. Hansen, J. N. Sørensen, S. Voutsinas andN. Sørensen, and H. Aa. Madsen. State of the art in wind turbine aerodynamics and aeroelasticity. *Progress in Aerospace Sciences*, 42:285–330, 2006.
20. F. M. Jensen, B. G. Falzon, J. Ankersen, and H. Stang. Structural testing and numerical simulation of a 34 m composite wind turbine blade. *Composite Structures*, 76:52–61, 2006.
21. J. Kiendl, Y. Bazilevs, M.-C. Hsu, R. Wüchner, and K.-U. Bletzinger. The bending strip method for isogeometric analysis of Kirchhoff–Love shell structures comprised of multiple patches. *Computer Methods in Applied Mechanics and Engineering*, 199:2403–2416, 2010.
22. Y. Bazilevs, M.-C. Hsu, J. Kiendl, and D. J. Benson. A computational procedure for prebending of wind turbine blades. *International Journal for Numerical Methods in Engineering*, 89:323–336, 2012.
23. D. Cárdenas, A. A. Escárpita, H. Elizalde, J. J. Aguirre, P. Marzocca H. Ahuett, and O. Probst. Numerical validation of a finite element thin-walled beam model of a composite wind turbine blade. *Wind Energy*, 15:203–223, 2012.
24. M.-C. Hsu, I. Akkerman, and Y. Bazilevs. Finite element simulation of wind turbine aerodynamics: Validation study using NREL Phase VI experiment. *Wind Energy*, 2012. In review.
25. Y. Bazilevs, M.-C. Hsu, J. Kiendl, R. Wüchner, and K.-U. Bletzinger. 3D simulation of wind turbine rotors at full scale. Part II: Fluid–structure interaction modeling with composite blades. *International Journal for Numerical Methods in Fluids*, 65:236–253, 2011.
26. Y. Bazilevs and T. J. R. Hughes. NURBS-based isogeometric analysis for the computation of flows about rotating components. *Computational Mechanics*, 43:143–150, 2008.
27. T. Tezduyar, S. Aliabadi, M. Behr, A. Johnson, V. Kalro, and M. Litke. Flow simulation and high performance computing. *Computational Mechanics*, 18:397–412, 1996.
28. M. Behr and T. Tezduyar. The Shear-Slip Mesh Update Method. *Computer Methods in Applied Mechanics and Engineering*, 174:261–274, 1999.
29. M. Behr and T. Tezduyar. Shear-slip mesh update in 3D computation of complex flow problems with rotating mechanical components. *Computer Methods in Applied Mechanics and Engineering*, 190:3189–3200, 2001.
30. T. E. Tezduyar. Finite element methods for flow problems with moving boundaries and interfaces. *Archives of Computational Methods in Engineering*, 8:83–130, 2001.
31. T. E. Tezduyar. Finite elements in fluids: Special methods and enhanced solution techniques. *Computers & Fluids*, 36:207–223, 2007.
32. Y. Bazilevs, M.-C. Hsu, and M. A. Scott. Isogeometric fluid–structure interaction analysis with emphasis on non-matching discretizations, and with application to wind turbines. *Computer Methods in Applied Mechanics and Engineering*, 2012. doi:10.1016/j.cma.2012.03.028.
33. T. J. R. Hughes, J. A. Cottrell, and Y. Bazilevs. Isogeometric analysis: CAD, finite elements, NURBS, exact geometry, and mesh refinement. *Computer Methods in Applied Mechanics and Engineering*, 194:4135–4195, 2005.
34. J. A. Cottrell, T. J. R. Hughes, and Y. Bazilevs. *Isogeometric Analysis: Toward Integration of CAD and FEA*. Wiley, Chichester, 2009.
35. T. E. Tezduyar, S. Sathe, J. Pausewang, M. Schwaab, J. Christopher, and J. Crabtree. Interface projection techniques for fluid–structure interaction modeling with moving-mesh methods. *Computational Mechanics*, 43:39–49, 2008.
36. T. E. Tezduyar, S. Sathe, J. Pausewang, M. Schwaab, J. Christopher, and J. Crabtree. Fluid–structure interaction modeling of ringsail parachutes. *Computational Mechanics*, 43:133–142, 2008.
37. K. Takizawa, C. Moorman, S. Wright, T. Spielman, and T. E. Tezduyar. Fluid–structure interaction modeling and performance analysis of the Orion spacecraft parachutes. *International Journal for Numerical Methods in Fluids*, 65:271–285, 2011.
38. K. Takizawa, S. Wright, C. Moorman, and T. E. Tezduyar. Fluid–structure interaction modeling of parachute clusters. *International Journal for Numerical Methods in Fluids*, 65:286–307, 2011.
39. K. Takizawa, T. Spielman, and T. E. Tezduyar. Space–time FSI modeling and dynamical analysis of spacecraft parachutes and parachute clusters. *Computational Mechanics*, 48:345–364, 2011.
40. K. Takizawa and T. E. Tezduyar. Computational methods for parachute fluid–structure interactions. *Archives of Computational Methods in Engineering*, 19:125–169, 2012.
41. Y. Bazilevs, M.-C. Hsu, K. Takizawa, and T. E. Tezduyar. ALE–VMS and ST–VMS methods for computer modeling of wind-turbine rotor aerodynamics and fluid–structure interaction. *Mathematical Models and Methods in Applied Sciences*, 2012. doi:10.1142/S0218202512300025.

42. K. Takizawa, Y. Bazilevs, and T. E. Tezduyar. Space–time and ALE-VMS techniques for patient-specific cardiovascular fluid–structure interaction modeling. *Archives of Computational Methods in Engineering*, 19:171–225, 2012.
43. Y. Bazilevs and T. J. R. Hughes. Weak imposition of Dirichlet boundary conditions in fluid mechanics. *Computers and Fluids*, 36:12–26, 2007.
44. M.-C. Hsu, I. Akkerman, and Y. Bazilevs. Wind turbine aerodynamics using ALE–VMS: Validation and the role of weakly enforced boundary conditions. *Computational Mechanics*, 2012. doi:10.1007/s00466-012-0686-x.
45. J. Kiendl, K.-U. Bletzinger, J. Linhard, and R. Wüchner. Isogeometric shell analysis with Kirchhoff–Love elements. *Computer Methods in Applied Mechanics and Engineering*, 198:3902–3914, 2009.
46. J. Nitsche. Uber ein variationsprinzip zur losung von Dirichlet-problemen bei verwendung von teilraumen, die keinen randbedingungen unterworfen sind. *Abh. Math. Univ. Hamburg*, 36:9–15, 1971.
47. P. Hansbo and J. Hermansson. Nitsche's method for coupling non-matching meshes in fluid-structure vibrational problems. *Computational Mechanics*, 32:134–139, 2004.
48. D. N. Arnold, F. Brezzi, B. Cockburn, and L. D. Marini. Unified analysis of Discontinuous Galerkin methods for elliptic problems. *SIAM Journal of Numerical Analysis*, 39:1749–1779, 2002.
49. Y. Bazilevs, V. M. Calo, Y. Zhang, and T. J. R. Hughes. Isogeometric fluid–structure interaction analysis with applications to arterial blood flow. *Computational Mechanics*, 38:310–322, 2006.
50. Y. Bazilevs, V. M. Calo, T. J. R. Hughes, and Y. Zhang. Isogeometric fluid–structure interaction: theory, algorithms, and computations. *Computational Mechanics*, 43:3–37, 2008.
51. Y. Bazilevs, J. R. Gohean, T. J. R. Hughes, R. D. Moser, and Y. Zhang. Patient-specific isogeometric fluid–structure interaction analysis of thoracic aortic blood flow due to implantation of the Jarvik 2000 left ventricular assist device. *Computer Methods in Applied Mechanics and Engineering*, 198:3534–3550, 2009.
52. Y. Bazilevs, M.-C. Hsu, D. Benson, S. Sankaran, and A. Marsden. Computational fluid–structure interaction: Methods and application to a total cavopulmonary connection. *Computational Mechanics*, 45:77–89, 2009.
53. Y. Bazilevs, M.-C. Hsu, Y. Zhang, W. Wang, X. Liang, T. Kvamsdal, R. Brekken, and J. Isaksen. A fully-coupled fluid–structure interaction simulation of cerebral aneurysms. *Computational Mechanics*, 46:3–16, 2010.
54. Y. Bazilevs, M.-C. Hsu, Y. Zhang, W. Wang, T. Kvamsdal, S. Hentschel, and J. Isaksen. Computational fluid–structure interaction: Methods and application to cerebral aneurysms. *Biomechanics and Modeling in Mechanobiology*, 9:481–498, 2010.
55. Y. Zhang, W. Wang, X. Liang, Y. Bazilevs, M.-C. Hsu, T. Kvamsdal, R. Brekken, and J.G. Isaksen. High-fidelity tetrahedral mesh generation from medical imaging data for fluid–structure interaction analysis of cerebral aneurysms. *Computer Modeling in Engineering & Sciences*, 42:131–150, 2009.
56. M.-C. Hsu and Y. Bazilevs. Blood vessel tissue prestress modeling for vascular fluid–structure interaction simulations. *Finite Elements in Analysis and Design*, 47:593–599, 2011.
57. C. C. Long, M.-C. Hsu, Y. Bazilevs, J. A. Feinstein, and A. L. Marsden. Fluid–structure interaction simulations of the Fontan procedure using variable wall properties. *International Journal for Numerical Methods in Biomedical Engineering*, 28:512–527, 2012.
58. A. N. Brooks and T. J. R. Hughes. Streamline upwind/Petrov-Galerkin formulations for convection dominated flows with particular emphasis on the incompressible Navier-Stokes equations. *Computer Methods in Applied Mechanics and Engineering*, 32:199–259, 1982.
59. T. J. R. Hughes and T. E. Tezduyar. Finite element methods for first-order hyperbolic systems with particular emphasis on the compressible Euler equations. *Computer Methods in Applied Mechanics and Engineering*, 45:217–284, 1984.
60. T. E. Tezduyar and Y. J. Park. Discontinuity capturing finite element formulations for nonlinear convection-diffusion-reaction equations. *Computer Methods in Applied Mechanics and Engineering*, 59:307–325, 1986.
61. T. J. R. Hughes, L. P. Franca, and M. Balestra. A new finite element formulation for computational fluid dynamics: V. Circumventing the Babuška–Brezzi condition: A stable Petrov–Galerkin formulation of the Stokes problem accommodating equal-order interpolations. *Computer Methods in Applied Mechanics and Engineering*, 59:85–99, 1986.
62. T. E. Tezduyar and Y. Osawa. Finite element stabilization parameters computed from element matrices and vectors. *Computer Methods in Applied Mechanics and Engineering*, 190:411–430, 2000.
63. T. E. Tezduyar. Computation of moving boundaries and interfaces and stabilization parameters. *International Journal for Numerical Methods in Fluids*, 43:555–575, 2003.
64. T. J. R. Hughes, G. Scovazzi, and L. P. Franca. Multiscale and stabilized methods. In E. Stein, R. de Borst, and T. J. R. Hughes, editors, *Encyclopedia of Computational Mechanics, Vol. 3, Fluids*, chapter 2. Wiley, 2004.
65. T. E. Tezduyar and S. Sathe. Modeling of fluid–structure interactions with the space–time finite elements: Solution techniques. *International Journal for Numerical Methods in Fluids*, 54:855–900, 2007.
66. Y. Bazilevs, V. M. Calo, J. A. Cottrel, T. J. R. Hughes, A. Reali, and G. Scovazzi. Variational multiscale residual-based turbulence modeling for large eddy simulation of incompressible flows. *Computer Methods in Applied Mechanics and Engineering*, 197:173–201, 2007.
67. M.-C. Hsu, Y. Bazilevs, V. M. Calo, T. E. Tezduyar, and T. J. R. Hughes. Improving stability of stabilized and multiscale formulations in flow simulations at small time steps. *Computer Methods in Applied Mechanics and Engineering*, 199:828–840, 2010.
68. Y. Bazilevs, C. Michler, V. M. Calo, and T. J. R. Hughes. Weak Dirichlet boundary conditions for wall-bounded turbulent flows. *Computer Methods in Applied Mechanics and Engineering*, 196:4853–4862, 2007.
69. Y. Bazilevs, C. Michler, V. M. Calo, and T. J. R. Hughes. Isogeometric variational multiscale modeling of wall-bounded turbulent flows with weakly enforced boundary conditions on unstretched meshes. *Computer Methods in Applied Mechanics and Engineering*, 199:780–790, 2010.
70. Y. Bazilevs and I. Akkerman. Large eddy simulation of turbulent Taylor–Couette flow using isogeometric analysis and the residual–based variational multiscale method. *Journal of Computational Physics*, 229:3402–3414, 2010.
71. Y. Bazilevs, V. M. Calo, J. A. Cottrell, J. A. Evans, T. J. R. Hughes, S. Lipton, M. A. Scott, and T. W. Sederberg. Isogeometric analysis using T-splines. *Computer Methods in Applied Mechanics and Engineering*, 199:229–263, 2010.
72. M. R. Dörfel, B. Jüttler, and B. Simeon. Adaptive isogeometric analysis by local *h*-refinement with T-splines. *Computer Methods in Applied Mechanics and Engineering*, 199:264–275, 2010.
73. F. Cirak, M. Ortiz, and P. Schröder. Subdivision surfaces: a new paradigm for thin shell analysis. *International Journal for Numerical Methods in Engineering*, 47:2039–2072, 2000.
74. F. Cirak and M. Ortiz. Fully C^1-conforming subdivision elements for finite deformation thin shell analysis. *International Journal for Numerical Methods in Engineering*, 51:813–833, 2001.
75. F. Cirak, M. J. Scott, E. K. Antonsson, M. Ortiz, and P. Schröder. Integrated modeling, finite-element analysis, and engineering design for thin-shell structures using subdivision. *Computer-Aided Design*, 34:137–148, 2002.

76. E. Oñate and F. Zarate. Rotation-free triangular plate and shell elements. *International Journal for Numerical Methods in Engineering*, 47:557–603, 2000.
77. E. Oñate and F. G. Flores. Advances in the formulation of the rotation-free basic shell triangle. *Computer Methods in Applied Mechanics and Engineering*, 194:2406–2443, 2005.
78. D. J. Benson, Y. Bazilevs, M.-C. Hsu, and T. J. R. Hughes. A large deformation, rotation-free, isogeometric shell. *Computer Methods in Applied Mechanics and Engineering*, 200:1367–1378, 2011.
79. N. Nguyen-Thanh, J. Kiendl, H. Nguyen-Xuan, R. Wüchner, K.U. Bletzinger, Y. Bazilevs, and T. Rabczuk. Rotation-free isogeometric thin shell analysis using PHT-splines. *Computer Methods in Applied Mechanics and Engineering*, 200:3410–3424, 2011.
80. C. Farhat, M. Lesoinne, and P. Le Tallec. Load and motion transfer algorithms for fluid/structure interaction problems with non-matching discrete interfaces: Momentum and energy conservation, optimal discretization and application to aeroelasticity. *Computer Methods in Applied Mechanics and Engineering*, 157:95–114, 1998.
81. K. Takizawa and T. E. Tezduyar. Multiscale space–time fluid–structure interaction techniques. *Computational Mechanics*, 48:247–267, 2011.
82. K. Takizawa and T. E. Tezduyar. Space–time fluid–structure interaction methods. *Mathematical Models and Methods in Applied Sciences*, 2012. To appear, DOI: 10.1142/S0218202512300013.
83. T. E. Tezduyar, S. Sathe, and K. Stein. Solution techniques for the fully-discretized equations in computation of fluid–structure interactions with the space–time formulations. *Computer Methods in Applied Mechanics and Engineering*, 195:5743–5753, 2006.
84. T. E. Tezduyar, S. Sathe, R. Keedy, and K. Stein. Space–time finite element techniques for computation of fluid–structure interactions. *Computer Methods in Applied Mechanics and Engineering*, 195:2002–2027, 2006.
85. J. Chung and G. M. Hulbert. A time integration algorithm for structural dynamics withimproved numerical dissipation: The generalized-α method. *Journal of Applied Mechanics*, 60:371–75, 1993.
86. K. E. Jansen, C. H. Whiting, and G. M. Hulbert. A generalized-α method for integrating the filtered Navier-Stokes equations with a stabilized finite element method. *Computer Methods in Applied Mechanics and Engineering*, 190:305–319, 2000.
87. T. E. Tezduyar, M. Behr, S. Mittal, and A. A. Johnson. Computation of unsteady incompressible flows with the finite element methods – space–time formulations, iterative strategies and massively parallel implementations. In *New Methods in Transient Analysis*, PVP-Vol.246/AMD-Vol.143, pages 7–24, New York, 1992. ASME.
88. T. Tezduyar, S. Aliabadi, M. Behr, A. Johnson, and S. Mittal. Parallel finite-element computation of 3D flows. *Computer*, 26(10):27–36, 1993.
89. A. A. Johnson and T. E. Tezduyar. Mesh update strategies in parallel finite element computations of flow problems with moving boundaries and interfaces. *Computer Methods in Applied Mechanics and Engineering*, 119:73–94, 1994.
90. J. M. Jonkman. Dynamics of offshore floating wind turbines–model development and verification. *Wind Energy*, 12:459–492, 2009.
91. J. M. Jonkman and D. Matha. Dynamics of offshore floating wind turbines–analysis of three concepts. *Wind Energy*, 14:557–569, 2011.
92. M. A. Lackner and M. A. Rotea. Passive structural control of offshore wind turbines. *Wind Energy*, 14:373–388, 2011.
93. P. J. Nicklasson M. C. Homola, M. S. Virk and P. A. Sundsbø. Performance losses due to ice accretion for a 5 MW wind turbine. *Wind Energy*, 15:379–389, 2012.
94. R. Chow and C. P. van Dam. Verication of computational simulations of the NREL 5 MW rotor with a focus on inboard ow separation. *Wind Energy*, 2011. doi:10.1002/we.529.
95. M. A. Lackner. An investigation of variable power collective pitch control for load mitigation of floating offshore wind turbines. *Wind Energy*, 2012. doi:10.1002/we.1500.
96. T. Sebastian and M. A. Lackner. Characterization of the unsteady aerodynamics of offshore floating wind turbines. *Wind Energy*, 2012. doi:10.1002/we.545.
97. M.-C. Hsu, I. Akkerman, and Y. Bazilevs. High-performance computing of wind turbine aerodynamics using isogeometric analysis. *Computers & Fluids*, 49:93–100, 2011.
98. M.-C. Hsu. *Fluid–Structure Interaction Analysis of Wind Turbines*. PhD thesis, University of California, San Diego, 2012.
99. E. Hau. *Wind Turbines: Fundamentals, Technologies, Application, Economics. 2nd Edition*. Springer, Berlin, 2006.